Applied Thermal Engineering 242 (2024) 122478

Contents lists available at ScienceDirect

Applied Thermal Engineering

journal homepage: www.elsevier.com/locate/apthermeng

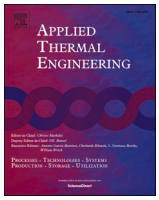

Research Paper

Numerical model for determining the effective heat capacity of macroencapsulated PCM for building applications

Matias Alvarez-Rodriguez [a,*], Mar Alonso-Martinez [a], Ines Suarez-Ramon [a], Paulino José García-Nieto [b]

[a] University of Oviedo, GICONSIME Research Group, C/Pedro Puig Adam s/n 33204, Gijón, Asturias, Spain
[b] University of Oviedo, Department of Mathematics, Faculty of Sciences, 33007, Oviedo, Asturias, Spain

ARTICLE INFO

Keywords:
Inverse method
Genetic algorithm
Effective heat capacity
Building material
Phase change modeling
Macroencapsulated phase change material

ABSTRACT

This paper presents a finite difference model of macroencapsulated PCM panels coupled with the genetic algorithm for the determination of effective heat capacity of whole panels via inverse method. This provides an accurate characterization of the thermal properties of macroencapsulated PCMs for building envelope applications. A novel definition of the effective heat capacity is proposed based on the superimposition of two Gaussian curves, applicable to any PCM whose phase transition is characterized by a single peak. Three PCMs were tested, subjected to temperature variation rates typically experienced in building envelopes: 0.5 °C/h and 1 °C/h. Surface temperature and heat flux were measured and used in the inverse method procedure. The developed model is accurate, as numerical results greatly agree with the experiments: the root mean square difference between the experimental and numerical heat fluxes ranged between 0.543 and 1.246 W/m^2. Significant differences in the effective heat capacity were found between the whole macrocapsule and small quantities of PCM (specified in the datasheets). The effective heat capacity specified in the datasheets is sensibly greater than that of the whole macrocapsules determined through the inverse method: the specific heat in the solid phase was up to 107.39 % higher in the datasheet values, the specific heat in the liquid phase up to 184.04 %, and the peak effective heat capacity, between 18.28 % and 164.11 %. The same happened to the enthalpy: datasheet values were 61.24 % – 175.55 % greater than inverse method results. This proves that latent heat is overestimated if small quantities of PCM are analyzed, and not the whole panels. The scale effect was assessed by comparing two capsules with the same material, but with different quantities of PCM: 0.5 kg and 1 kg. A greater mass of PCM over the total mass of the capsule implies a different relationship between the effective heat capacity and temperature, with higher peak heat capacity. The capsule with 1 kg of PCM showed a peak effective heat capacity up to 30.65 % greater than that of the panel with 0.5 kg of PCM. Thus, adequate modeling in building applications requires characterization of whole macroencapsulated PCMs. The determination of the relationship between temperature and effective heat capacity of macroencapsulated PCMs presented in this work could easily be incorporated into other simulation software, facilitating the assessment of adaptive envelopes with PCM macrocapsules.

1. Introduction

Great concern exists about climate change worldwide, with a strong focus on research about the reduction of energy consumption of buildings, as they account for 34 % of final energy consumption and 37 % of CO_2 emissions globally [1]. To minimize energy consumption in buildings, several actions are internationally investigated: reduction of the effect of solar gains on envelopes using reflective coatings, development of new insulation solutions, use of air cavities in walls to minimize thermal transmittance or, more recently, the addition of phase change materials (PCMs) into building envelopes [2].

PCMs take advantage of the latent heat absorbed and released during the phase change process at a certain temperature or temperature range. The incorporation of PCMs into building envelopes is a latent heat thermal energy storage technique that reduces energy demand, stabilizes indoor temperature and increases thermal comfort [3]. These materials accumulate larger amounts of thermal energy per unit or mass or

* Corresponding author.
E-mail address: alvarezrmatias@uniovi.es (M. Alvarez-Rodriguez).

https://doi.org/10.1016/j.applthermaleng.2024.122478
Received 25 September 2023; Received in revised form 19 December 2023; Accepted 15 January 2024
Available online 19 January 2024

Nomenclature

a	Height [m]
Cp	Specific heat [J/kg·K]
Cp_{eff}	Effective heat capacity [J/kg·K]
e	Thickness [m]
h	Specific enthalpy [J/kg]
k	Thermal conductivity [W/m·K]
m	Mass [kg]
N	Number of cells
N_t	Number of time steps
T	Temperature [°C]
t	Time [s]
w	Width [m]
$\vec{x}$	Vector of parameters that defines the effective heat capacity

Greek letters

α	Heating/cooling rate [°C/h]
ρ	Density [kg/m^3]
φ	Heat flux on the mortar layer surface [W/m^2]
σ	Parameter for the width of the curve of effective heat capacity [K^2]
τ	Duration of experiment [s]
ΔC	Parameter for maximum height of curve of effective heat capacity [J/kgK]
Δt	Data sampling period [s]
Δx	Thickness of the cells [m]

Subscript

L	Liquid phase
lower	Lower limit of the genetic algorithm search space
Mt	Mortar layer
n	Cell number index
new	Current iteration
o	Surface of the mortar layer
old	Previous iteration
opt	Optimum solution found by the genetic algorithm
PCM	Whole PCM panel
ref	Reference for setting the zero enthalpy value
S	Solid phase
sw	Switching point between symmetric and asymmetric Gaussian curves
upper	Upper limit of the genetic algorithm search space

Superscript

exp	Experimental value
∕	Symmetric curve of effective heat capacity
h	Asymmetric curve of effective heat capacity
M	Melting
num	Determined with the numerical model
S	Solidification
t	Current time step
t-1	Previous time step

Acronyms

DAT	Datasheet values
DSC	Differential scanning calorimetry
FDM	Finite difference method
GA	Genetic algorithm
IV	Inverse method results
OF	Objective function
PCM	Phase change material
RMSD	Root mean square difference
THM	Temperature-history method

volume, compared to sensible heat storage [4]. However, not all PCMs are adequate for this application. For building purposes, PCMs should have high latent heat, high specific heat capacity, small volume changes, non-corrosiveness, non-toxicity, non-flammability, little or no decomposition or subcooling, and a reasonable price and availability on the market [5].

Several factors affect the thermal response of PCMs incorporated in building envelopes. The phase change temperature or temperature range is a key factor. The International Energy Agency in the Annual Report of 2022 indicated that the suitable phase change temperature range for building applications is 18 – 30 °C to ensure thermal comfort [6]. The incorporation method also affects the thermal performance of PCMs in the building envelope. PCMs are incorporated either by being integrated into construction materials (gypsum, cement, mortar, concrete or insulation) through direct incorporation, impregnation or microencapsulation [7]; or as a layer of the wall as macroencapsulated [8] or shape-stabilized [9] PCMs. Macroencapsulation stands as a promising option, as it allows easy incorporation, avoids direct contact between the PCMs and the construction materials, improves heat transfer, prevents leakage and is convenient for transportation and packaging [10]. It consists of containing the PCMs inside capsules whose size is greater than 1 mm or 1 cm (threshold limits vary depending on the source) that come in different shapes, sizes and materials [11]. One of the preferred solutions for incorporation in the building envelope is thin metallic panels in vertical disposition [12]. On top of this, it has also been demonstrated that the position of the PCM elements in the envelope is a key factor in energy consumption reduction [13].

Experimental studies illustrate the energy saving potential of PCMs in building walls. However, experiments are time-consuming and expensive. In addition, the wide variety of existing PCMs, possible incorporation methods, wall design configurations, climatic conditions and interior conditions create a gap of knowledge in the selection of the most adequate PCM and wall typology [14]. Mathematical modeling stands as an effective tool to tackle this complex optimization problem, without performing experimental tests, reducing costs and time of study [15].

The enthalpy method and the effective heat capacity method are two well-known techniques for modeling phase change in building applications among others. They rely on establishing a relationship between enthalpy and temperature or heat capacity and temperature, respectively, for integrating the latent heat exchange. Several studies where these models have been used can be found in [16]. In short, these techniques do not explicitly track the phase change front, but the interface condition is implicitly incorporated in the set of equations that is being solved. To ensure that models predict the real behavior of PCMs in building envelope applications, the thermophysical properties of PCMs need to be defined [17]. Differential scanning calorimetry (DSC) and temperature-history method (THM) are typically used to determine the thermophysical properties of PCMs. There exist limitations to these widely used methods. Typical weight of samples in DSC is in the range of micrograms to milligrams. This leads to significant discrepancies when properties determined though DSC are used for modelling systems with a greater mass of PCM [18]. THM characterizes samples of up to 15 g [19], this is, a thousand times bigger than those in DSC. Nonetheless, this size still does not represent the behavior of macroencapsulated PCMs in building applications, ranging from 200 g [20] to 7 kg [21]. On top of that, heating and cooling rates in DSC affect the measured heat flux and phase change temperature [22]. These range from 1 °C/min to

10 °C/min, making the DSC a quick method. However, these rates are a lot higher than those occurring in real building applications [22]. These limitations have led authors to research unconventional methods for an accurate determination of the thermophysical properties of PCMs. The inverse method coupled with an optimization algorithm stands as a possible approach to estimate the enthalpy or heat capacity relationship with temperature.

The inverse method applied to heat transfer problems consists of determining the thermal properties of a material, boundary conditions or internal heat source values based on experimentally measured temperatures and/or heat fluxes at a finite number of locations. This differs from classic heat transfer problems, where temperature distribution is calculated by solving governing equations and knowing the thermal properties of materials and boundary conditions [23]. The experimental measurements and the values determined by the classic or direct model are linked through an objective function, typically defined as the deviation between experimental and modeled results. As the inverse method is computationally intensive, there exist different optimization methods applied to heat transfer models of PCMs to estimate heat capacity and enthalpy relationship with temperature [24].

The inverse method was applied to the results of traditional characterization methods to determine the heat capacity-temperature and/or enthalpy-temperature curves. Franquet *et al.* [25] employed the inverse method on the results of DSC experiments of pure substances and binary mixtures for estimating thermodynamic properties, based on thermodynamic and heat transfer modelling of the samples. The objective function they minimized is the sum of squared differences between experimentally measured heat flux and modelled values. This objective function was minimized through the simplex method. Omaraa *et al.* [24] performed the THM to pure zinc and sodium nitrate and then used the inverse method to obtain the heat capacity-temperature. The phase change was modelled with a symmetric Gaussian curve for heat capacity-temperature and the heat transfer in the samples with a 1D finite difference model. The objective function was the root mean square difference (RMSD), using the central temperature of the sample for minimization. Generalized Reduced Gradient nonlinear optimization method was selected for minimization. Delcroix *et al.* [26] also employed THM results with the inverse method coupled with genetic algorithm for the determination of the heat capacity-temperature curve of a bio-based PCM, as well as the phase change range. RMSD of measured and modeled temperature in the center of the samples was set as the objective function for optimization. Two curves were obtained, one for melting and the other for solidification, consisting of a step function depending on temperature intervals (7 for melting and 9 for solidification). The phase change range determined through the inverse method was wider than the one obtained through DSC. On top of that, the authors also determined the equivalent effective heat capacity curve for a wall formed by a layer of PCM pouches sandwiched between plywood boards, concluding that for such building applications, DSC or THM results are not directly applicable and other experimental tests should be used.

The inverse method was also used for the determination of properties of composite materials integrating PCMs. Tittelein *et al.* [27] determined the phase change enthalpy and the enthalpy-temperature curve for a composite of cement and microencapsulated PCM (Micronal PCM ® DS 5001 X by BASF), of dimensions 250 x 250 x 40 mm^3. A 1D finite volume method was developed to solve the conduction in the samples. Heat flux on the surfaces of the sample was used for the objective function. This function was set as the quadratic sum of the differences between measured and calculated surface heat flux and simplex algorithm was used for the minimization. Cheng *et al.* [28] determined the heat capacity-temperature curve of a concrete brick with microencapsulated PCMs coupling experiments with a 1D finite difference model of the heat transfer. The curve was defined by intervals of temperature. Different optimization methods were compared: sequential quadric programming, particle swarm optimization and genetic optimization. Cascone *et al.* [29] calculated the heat capacity-temperature curve of a 15 mm shape-stabilized PCM of melting temperature 21.7 °C, through inverse method coupled with the ($\lambda + \mu$) Evolution Strategy technique. The curve was defined as an asymmetric Gaussian function, and it was the same for solidification and melting. A 1D finite difference model was developed to simulate heat transfer in the PCM. RMSD was chosen as the objective function, comparing the experimental and numerical values of heat flux.

There exist fewer studies of the determination of phase change properties of macroencapsulated PCMs. Thonon *et al.* [30] proposed a complex four-step identification process based on a comprehensive numerical model for solving heat transfer on a paraffin macroencapsulated in a PMMA rectangular panel. The chosen objective function was the sum of squared differences in surface heat flux, and particle swarm optimization algorithm was used. Zalesak *et al.* [31] determined heat capacity-temperature curves of macroencapsulated paraffin RT42 separately for melting and solidification, defined as asymmetric Gaussian curves. PCM panels were tested inside an air heat exchanger, where the output air temperature was used for the objective function error minimization. Heat transfer in the PCM capsules was studied though a 1D model. Particle swarm optimization and differential evolution algorithms were employed for the optimization step. In the heat exchanger unit, the PCMs were subjected to sudden changes of temperature which do not apply to building envelope applications.

To the best knowledge of the authors, the application of the inverse method to determine the effective heat capacity of whole macroencapsulated PCM panels with heating and cooling rates typical of building envelopes has not been performed. Previous studies revealed that the incorporation of macroencapsulated PCMs in building envelopes reduces energy consumption. Still, there is a lack of comprehensive characterization of the whole macrocapsules, as it has been proved that DSC and THM results are not appropriate for full size applications [18]. This work proposes a mathematical model of the heat transfer in macroencapsulated PCMs for the determination of the effective heat capacity of full-size capsules through the inverse method. This yields the relationship between the effective heat capacity and temperature of the whole capsule taking into account the PCM itself, the capsule material, and the air gap left inside the capsule that allows volume changes. This analysis was developed for complete melting and solidification and, hence, hysteresis was identified. For the analysis of incomplete or interrupted phase transitions, the reader is referred to the following works: [32] experimentally analyzed the resulting enthalpy-temperature curves of different PCMs (paraffin mixtures, fatty acids and inorganic salts) for incomplete phase transitions; [33] developed a numerical model of incomplete phase transition simulation for PCMs with and without subcooling. Other authors developed a numerical hysteresis model where the enthalpy-temperature relationship for incomplete phase transitions was derived from the complete transition curves [34].

The main novelty of this work is that whole PCM panels are characterized for low heating and cooling rates. The contribution is a numerical tool that determines the effective heat capacity of PCM panels, so they may be modeled as unique building materials. The obtained results are suitable for whole building energy simulation software to assess the impact of adding PCM macrocapsules on the indoor temperature and energy consumption.

2. Materials and methods

2.1. Studied materials

This work analyzes paraffin mixtures macroencapsulated in aluminum containers: RT8-HC, RT11-HC, RT21-HC [35]. These are solid–liquid shifting PCMs and, since they are mixtures, they undergo phase change throughout a temperature range. The number in the name of these PCMs refers to the average phase change temperature. The

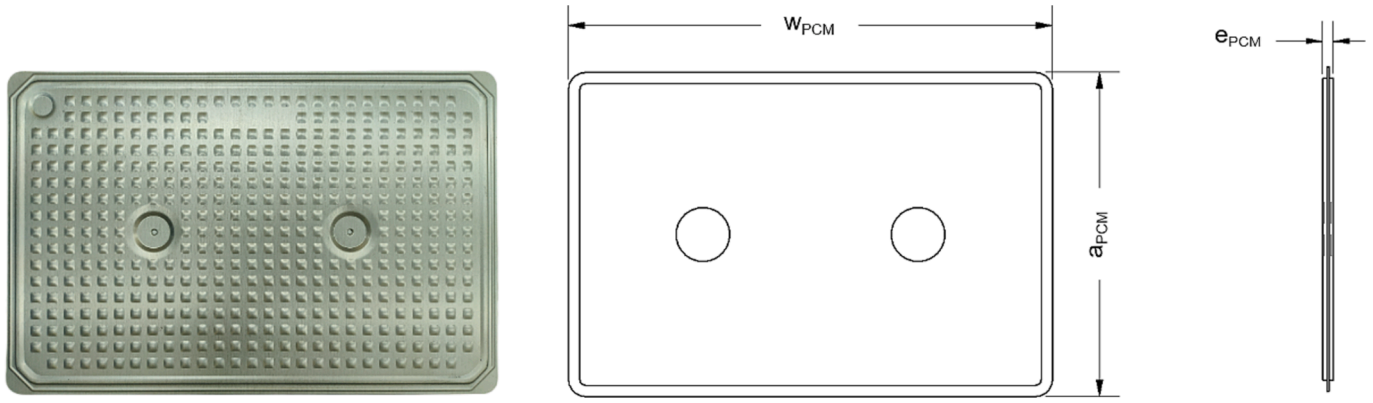

Fig. 1. Aluminum case containing the PCM.

Table 1
Geometry and mass of the studied PCM panels.

PCM	w_{PCM} (mm)	a_{PCM} (mm)	e_{PCM} (mm)	m_{PCM} (kg)
RT8-HC	450	300	10	0.85
RT8-HC	450	300	15	1.33
RT11-HC	450	300	10	0.85
RT21-HC	450	300	10	0.85

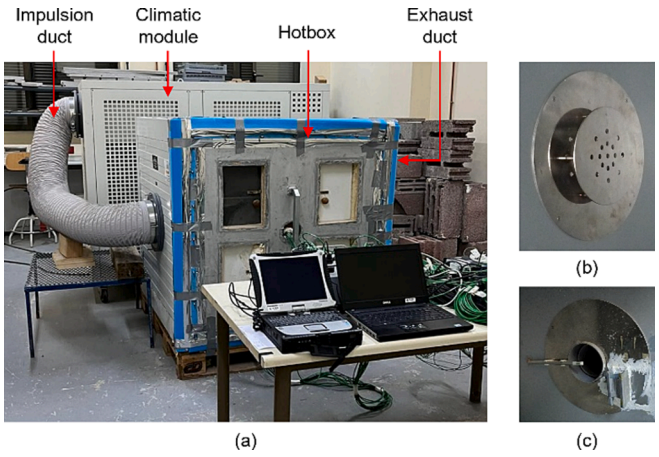

Fig. 2. Climatic module and hotbox: (a) general disposition, (b) detail of the diffuser in the impulsion duct, (c) detail of the probe in the exhaust duct.

manufacturer indicates in the product datasheets the phase change temperature range of the PCMs.

The aluminum capsule is shown in Fig. 1, where it must be observed that the surface of the panel is not flat but contains regularly distributed small bumps. This is the commercial macrocapsule supplied by the manufacturer [36]. A simplified blueprint of the capsule is also displayed, indicating the characteristic dimensions of the capsule: width, *w*, height, *a*, and thickness, *e*. It is highlighted that these macrocapsules consist of paraffins, an air gap to allow the volume variation during the phase change and the aluminum case itself. This has been considered in this work and from now on the subscript "PCM" will denote the whole panel (including paraffin, air and aluminum). Table 1 sums up the dimensions and mass, *m*, of the panels. Note that PCM RT8-HC is analyzed for two different capsule thicknesses.

2.2. Experimental setup

The PCM panels were tested in a hotbox connected to a climatic module in a closed loop. The hotbox consists of a 1 m × 1 m × 1 m highly insulated cavity, whereas the climatic module controls temperature and relative humidity of air inside the hotbox ranging from −20 °C to 60 °C and from 30 % to 100 %, respectively. Air is injected inside the hotbox through an impulsion duct that counts on a diffuser that ensures a uniform temperature distribution inside the chamber. An exhaust duct takes back the air into the climatic chamber, and it is provided with a probe for the temperature and relative humidity regulation. This equipment is shown in Fig. 2.

Experimental tests characterize PCM panels suspended vertically inside the hotbox, applying a temperature variation curve to the surrounding air, between 20 °C and 1 °C for RT8-HC and RT11-HC, and between 28 °C and 8 °C for RT21-HC. Transient evolution of temperature and heat flux of the panels is measured for two temperature variation rates, α, 1 °C/h and 0.5 °C/h. These are based on heating and cooling rates experienced in building envelopes. The selected vertical disposition stems from the fitness of these panels to vertical elements of the envelopes, such as façades, as it has been reported in the literature.

Macroencapsulated PCMs inside the hotbox were subjected to heating and cooling cycles, defined by 4 stages:

(1) solidification,
(2) thermal stabilization in solid phase,
(3) melting, and
(4) thermal stabilization in liquid phase.

This process provides the thermal performance of the macroencapsulated PCMs during the phase change, as well as for solid and liquid phases. Each test was repeated three times so that a high level of confidence in the experimental setup and repeatability were ensured. Temperature and heat flux were measured every 10 min (data sampling period $\Delta t = 600s$). Fig. 3 shows the programmed temperature curves in the climatic module, T_{prog}, for all studied PCM panels. The phase change temperature range of the pure paraffins, according to the manufacturer, is also included. Additionally, the four stages of the programmed curve are indicated.

Since the surface of the aluminum capsule is not flat, as seen in Fig. 1, it was not possible to directly place a heat flux sensor over it. As such, each surface of the PCM panels was covered with a thin layer of mortar (hereon identified by the subscript *Mt*) of thickness 6 mm, e_{Mt}. The apparent density or the mortar, ρ_{Mt}, was 2194.141 kg/m^3. This is the density of the mortar layer taking into account the mortar itself, and the pores of air. A TCi Thermal Conductivity Analyzer [37] was used for the determination of the thermal conductivity, k_{Mt}, and specific heat, Cp_{Mt}. This equipment uses the modified transient plane source technique to determine these properties and provides an accuracy of the measurements of 5 %. Thermal conductivity was 1.405 W/mK and specific heat 897.862 J/kgK.

Heat flux sensors and thermocouples were used to measure the transient thermal response of the panels. An HFP01 heat flux sensor [38] was added to the surface of the mortar of each PCM panel, measuring the

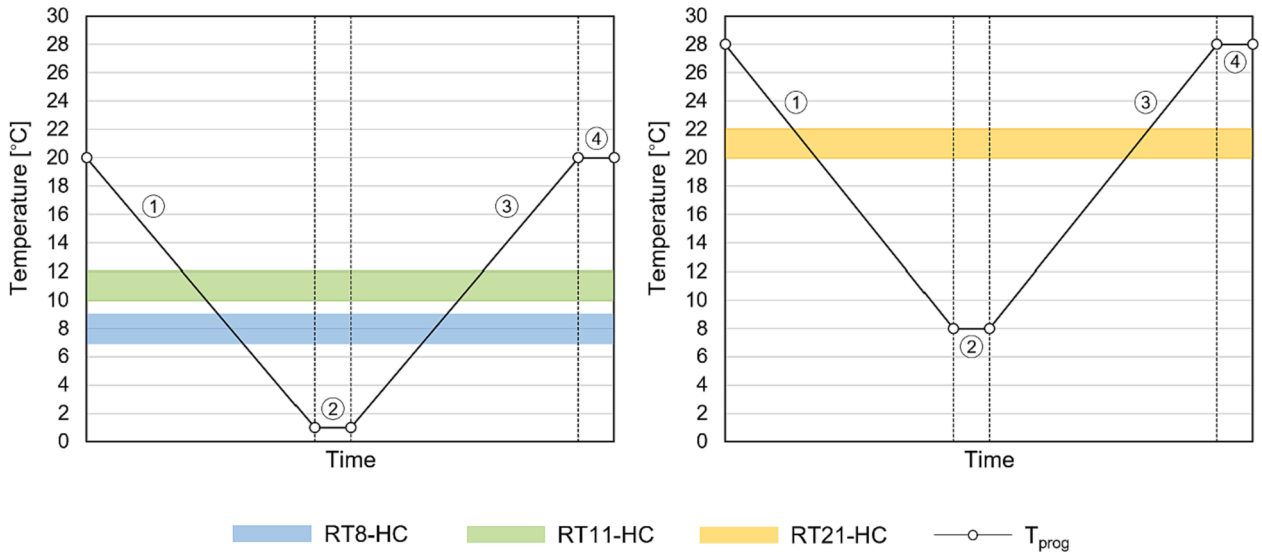

Fig. 3. Programmed temperatures in the hotbox for each PCM panel and phase change ranges.

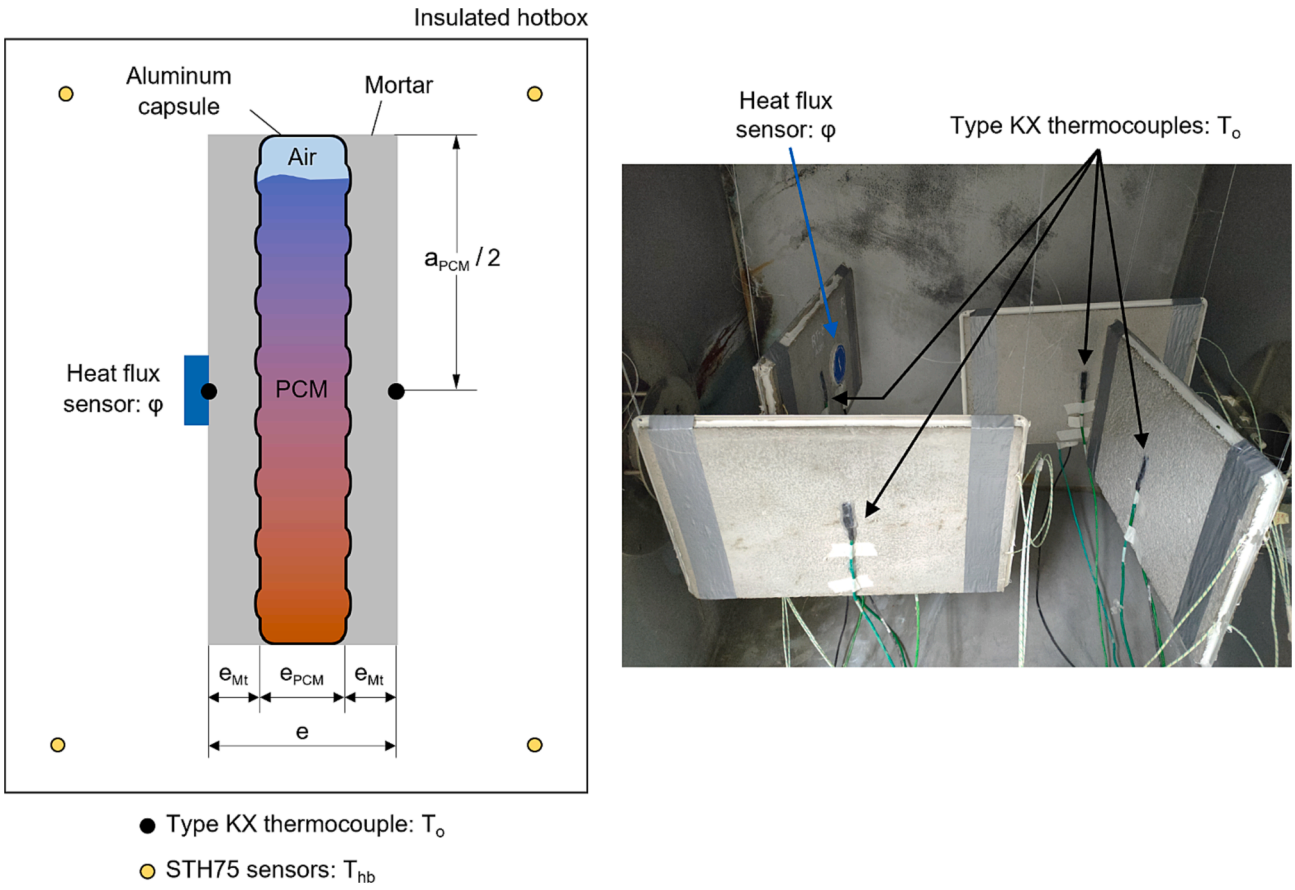

Fig. 4. Scheme of the experimental setup (left) and disposition of multiple panels inside the hotbox (right).

surface heat flux φ^{exp}. These are ceramics-plastic thin sensors, whose measuring uncertainty is 3 %. Only one heat flux sensor was used because of the symmetric disposition of the PCM panels and since a uniform temperature distribution inside the hotbox is ensured. One KX thermocouple was used for measuring the temperature on each surface of the panel, T_o^{exp}. These thermocouples provide ± 0.1 °C accuracy [38]. Temperature of the hotbox was also measured, for the sake of verification, with four STH75 sensors [39] placed in different locations of the chamber. Their accuracy is ± 0.15 °C and ± 0.9 %RH. Fig. 4 shows the position of all the sensors, and a schematic of the PCM panel–mortar layer assembly. It also shows how the panels were placed inside the hotbox.

2.3. Computational procedure

This subsection presents the mathematical model developed for the

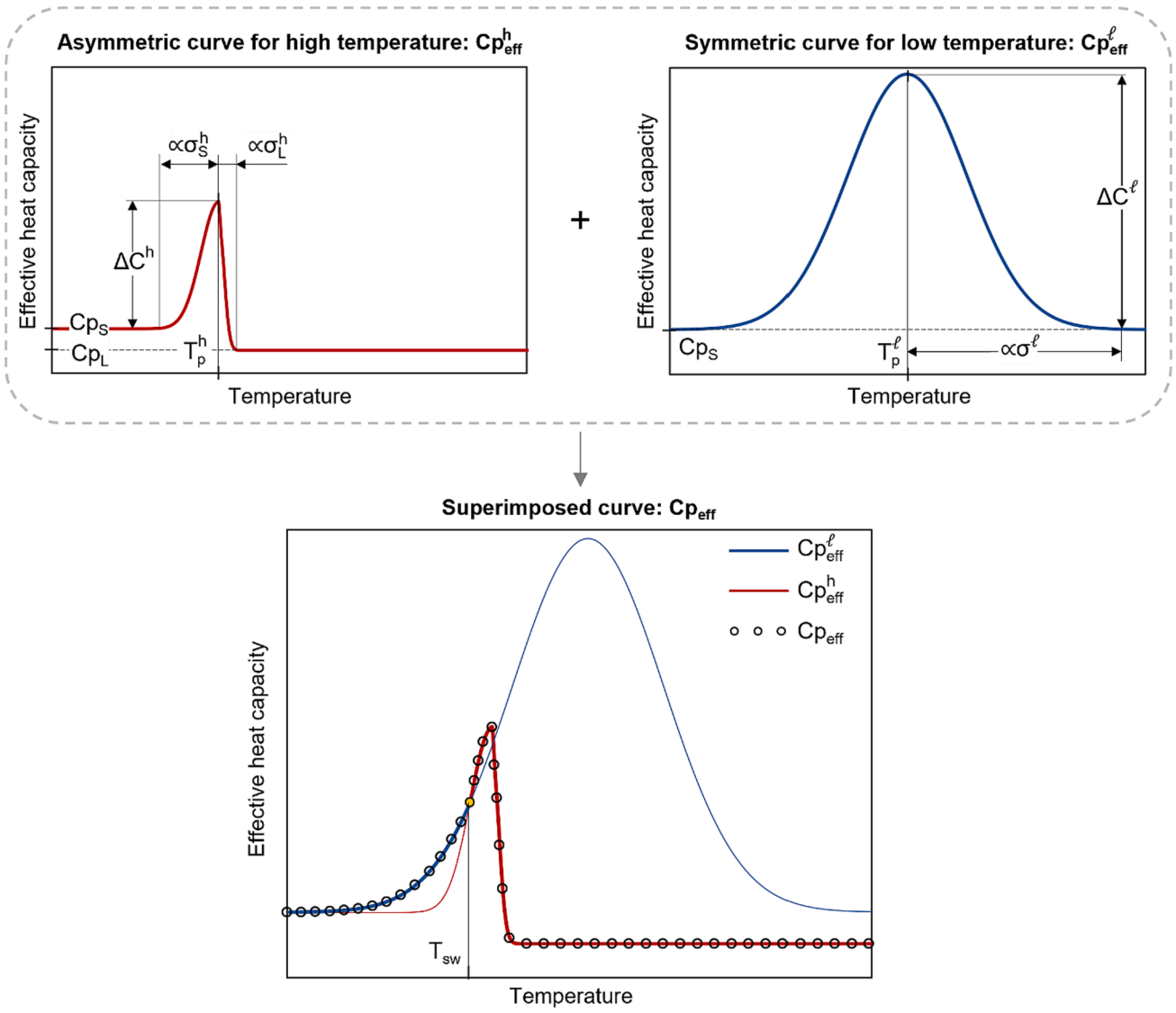

Fig. 5. Definition of the superimposed curve of effective heat capacity.

identification of the effective heat capacity of studied PCM panels. All calculations have been performed in MATLAB software [40]: own code was developed for the direct model, whereas the built-in Global Optimization Toolbox was used for the optimization stages [41].

2.3.1. Direct problem

Since this work aims to obtain the phase change properties of the whole PCM panels, these are modeled as a single material, lumping the effects of the aluminum capsule, air gap and paraffin altogether. The effects of the convection of the liquid phase and the air gap inside the panel on the thermal response are recorded in the temperature and heat flux measurements. As such, they are incorporated in the model though the boundary conditions. This is, all the physical phenomena that occur in the capsule are experimentally measured and, in consequence, considered in the model. As a result, transient heat transfer is modeled through the heat diffusion equation, requiring low computational cost but providing great accuracy:

$$\frac{\partial}{\partial t}(\rho CpT) = \nabla(k\nabla T) \tag{1}$$

where ∇ is the nabla operator. The effective heat capacity method is used for modeling the phase change in the PCM panel. Note that for the PCM panel, the specific heat in Eq. (1) is substituted by the effective heat capacity, Cp_{eff}, that varies with temperature.

The following assumptions have been made:

- Thermal contact resistance at the mortar-capsule interface is negligible.
- Thermophysical properties of the mortar layer are not dependent on temperature and are isotropic [42].
- Thermal conductivity of the PCM provided by the manufacturer will be used as input for the model. Thus, this is not a parameter that the optimization algorithm must determine in the inverse problem. This assumption is based on the parametric analysis of heat flux output performed on various PCMs in [25]. This work points out the phase change range and the latent energy as the most influencing parameters, and not the thermal conductivity, especially for low temperature variation rates. As such, thermal conductivity of the panels used in the model is $k_{PCM} = 0.2 W/mK$ [35].
- Density of the PCM panel is constant. Although density of the solid and liquid phases of the paraffin varies with the phase change, the panel as a whole is characterized. This implies that an overall density of the panel might be used, which is not dependent on temperature. Overall PCM panel density is thus calculated based on panel mass and volume, derived from data presented in Table 1.

- Heat transfer is one-dimensional. This hypothesis is justified by the reduced thickness of the capsules, compared to the heat exchange surface. Besides, the low thickness and uniform temperature applied to both sides of the PCM panels limit the convection occurring in the liquid phase. This assumption is also present in [30].
- Only half of the panel and one mortar layer are necessary for the mathematical model, due to the symmetry in the PCM panel plus mortar layers and boundary conditions.
- According to previous studies, Cp_{eff} is assumed to be shaped by a Gaussian function [31].

To obtain the best fitting, in this work Cp_{eff} is assumed to be shaped as two superimposed Gaussian functions: a symmetric one for lower values of temperature, $Cp^{\swarrow}_{eff}$, and an asymmetric one for higher values of temperature, Cp^{h}_{eff}:

$$Cp^{\swarrow}_{eff}(T) = Cp_S + \Delta C^{\swarrow} \cdot \exp\left(\frac{\left(T - T^{\swarrow}_p\right)^2}{\sigma^{\swarrow}}\right) \tag{2}$$

$$Cp^{h}_{eff}(T) = \begin{cases} Cp_S + \Delta C^{h} \cdot exp\left(\dfrac{\left(T - T^{h}_p\right)^2}{\sigma^{h}_S}\right) & if\ T \le T^{h}_p \\ Cp_L + \Delta C^{h} \cdot exp\left(\dfrac{\left(T - T^{h}_p\right)^2}{\sigma^{h}_L}\right) & if\ T > T^{h}_p \end{cases} \tag{3}$$

$$Cp_{eff}(T) = \begin{cases} Cp^{\swarrow}_{eff}(T) & if\ T \le T_{sw} \\ Cp^{h}_{eff}(T) & if\ T > T_{sw} \end{cases} \tag{4}$$

where Cp_S is the specific heat of the solid phase, Cp_L is the specific heat of the liquid phase, ΔC is the parameter that defines the maximum height of the curve, T_p is the temperature where the maximum effective heat capacity is reached, σ is the parameter that defines the width of the curve and T_{sw} is the temperature that defines the switching between each curve. Superscript $\swarrow$ refers to the symmetric curve for lower temperatures and superscript h refers to the asymmetric curve for higher temperatures. Subscript S indicates solid phase, whereas subscript L indicates liquid phase. Note that the parameter σ for the asymmetric curve takes two values: one for $T \le T_p$ and another for $T > T_p$, so that asymmetry is captured. The differences between $Cp^{\swarrow}_{eff}$ and Cp^{h}_{eff}, as well as their superimposition are illustrated in Fig. 5.

Additionally, the behavior of the PCM panels might be different in melting and in solidification. To identify these possible differences, it is necessary to define the parameters of the superimposed $Cp_{eff}(T)$ curve for solidification, superscript S, and for melting, superscript M, separately. As such, the vector of parameters $\vec{x}$ that defines the $Cp_{eff}(T)$ curve for both processes is:

$$\vec{x} = \left[Cp_S, Cp_L, \Delta C^{h,S}, \sigma^{h,S}_S, \sigma^{h,S}_L, T^{h,S}_p, \Delta C^{\swarrow,S}, \sigma^{\swarrow,S}, T^{\swarrow,S}_p, \Delta C^{h,M}, \sigma^{h,M}_S, \sigma^{h,M}_L, T^{h,M}_p, \Delta C^{\swarrow,M}, \sigma^{\swarrow,M}, T^{\swarrow,M}_p\right] \tag{5}$$

Note that Cp_S and Cp_L are independent of the phase change process since their values do not affect the phase change.

It is highlighted also that T_{sw} is not a parameter that has to be defined beforehand, but it is determined analytically, as it represents the temperature that fulfills the condition:

$$Cp^{\swarrow}_{eff}(T_{sw}) = Cp^{h}_{eff}(T_{sw}) \quad \forall T_{sw} \le T^{h}_p \tag{6}$$

This is, it is the point where the symmetric curve and the asymmetric curve (for $T \le T^{h}_p$) are coincident. Rearranging Eq. (6) a quadratic equation is reached, whose solution is:

$$T_{sw} = \frac{\sigma^{h}T^{\swarrow}_p - \sigma^{\swarrow}T^{h}_p - \sqrt{\left(\sigma^{h}T^{\swarrow}_p - \sigma^{\swarrow}T^{h}_p\right)^2 - \left(\sigma^{h} - \sigma^{\swarrow}\right)\left(\sigma^{h}T^{\swarrow 2}_p - \sigma^{\swarrow}T^{h2}_p - \sigma^{h}\sigma^{\swarrow}\ln\left(\frac{\Delta C^{h}}{\Delta C^{\swarrow}}\right)\right)}}{\sigma^{h} - \sigma^{\swarrow}} \tag{7}$$

The actual value of T_{sw} is obtained by subtracting the discriminant in Eq. (7), and not by adding it, as the switching point is found on the left side of the $Cp^{h}_{eff}(T)$ curve.

As it is well known, the heat diffusion equation must be completed with the initial temperature condition, along with the boundary conditions. The initial condition consists of setting the whole domain at the temperature measured on the surface at $t = 0$. Thermal stabilization stages before the heating and cooling ramps ensure uniform temperatures in the samples in the beginning of each process. Boundary conditions are described through Eqs. (8)-(10) below. These are, respectively, temperature condition in the mortar layer surface, conjugate heat transfer in the mortar–capsule interface and symmetry condition along the axis.

$$T(0,t) = T^{exp}_o(t) \tag{8}$$

$$-k_{Mt}\frac{\partial T(e_{Mt},t)}{\partial x} = -k_{PCM}\frac{\partial T(e_{Mt},t)}{\partial x} \tag{9}$$

$$-k_{PCM}\frac{\partial T(e/2,t)}{\partial x} = 0 \tag{10}$$

Finite difference method (FDM) is employed for solving the heat diffusion equation. To do so, the simulation domain is discretized in N cells whose thickness is Δx. The total number of N cells encompasses mortar cells, N_{Mt}, and PCM panel cells, N_{PCM}, as indicated in Eq. (11). The heat transfer equation (1) is then solved in each of these N cells at each time step. Fig. 6 shows a scheme of the discretized simulation domain, as well as these boundary conditions.

$$N = N_{PCM} + N_{Mt} \tag{11}$$

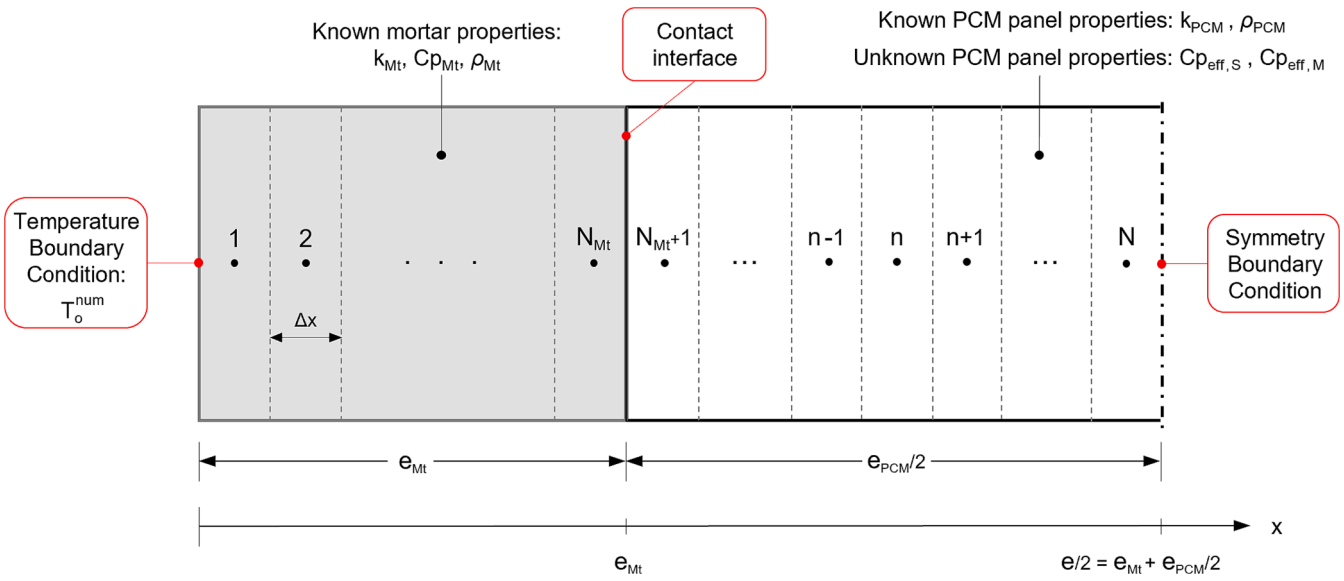

Fig. 6. Scheme of the 1D discretized simulation domain and boundary conditions.

In this study, a time-regressive (backward in time) finite-difference scheme and a space-centered finite difference scheme have been used to solve the heat diffusion equation to ensure that the numerical scheme is unconditionally stable. As such, and considering the boundary conditions, the equations for the temperature at each node n and at each time step t, T_n^t, are given by:

- Surface ($n = 1$):

$$\rho_{Mt}\cdot Cp_{Mt}\cdot\frac{T_n^t - T_n^{t-1}}{\Delta t} = k_{Mt}\cdot\left(\frac{T_{n+1}^t - T_n^t}{\Delta x^2} - \frac{T_n^t - T_o^{exp,t}}{\Delta x^2/2}\right) \tag{12}$$

- Interior node of the mortar ($1 < n < N_{Mt}$):

$$\rho_{Mt}\cdot Cp_{Mt}\cdot\frac{T_n^t - T_n^{t-1}}{\Delta t} = k_{Mt}\cdot\left(\frac{T_{n+1}^t - T_n^t}{\Delta x^2} - \frac{T_n^t - T_{n-1}^t}{\Delta x^2}\right) \tag{13}$$

- Interface node on the mortar side ($n = N_{Mt}$):

$$\rho_{Mt}\cdot Cp_{Mt}\cdot\frac{T_n^t - T_n^{t-1}}{\Delta t} = k_{Mt}\cdot\left(\frac{T_{n+1}^t - T_n^t}{\Delta x^2}\cdot\frac{2k_{PCM}}{k_M + k_{PCM}} - \frac{T_n^t - T_{n-1}^t}{\Delta x^2}\right) \tag{14}$$

- Interface node on the PCM panel side ($n = N_{Mt} + 1$):

$$\rho_{PCM}\cdot Cp_{eff}\left(T_n^t\right)\cdot\frac{T_n^t - T_n^{t-1}}{\Delta t} = k_{PCM}\cdot\left(\frac{T_{n+1}^t - T_n^t}{\Delta x^2} - \frac{T_n^t - T_{n-1}^t}{\Delta x^2}\cdot\frac{2k_{Mt}}{k_M + k_{PCM}}\right) \tag{15}$$

- Interior node of the PCM panel ($n_{Mt} + 1 < n < N$):

$$\rho_{PCM}\cdot Cp_{eff}\left(T_n^t\right)\cdot\frac{T_n^t - T_n^{t-1}}{\Delta t} = k_{PCM}\cdot\left(\frac{T_{n+1}^t - T_n^t}{\Delta x^2} - \frac{T_n^t - T_{n-1}^t}{\Delta x^2}\right) \tag{16}$$

- Symmetry node ($n = N$):

$$\rho_{PCM}\cdot Cp_{PCM}\left(T_n^t\right)\cdot\frac{T_n^t - T_n^{t-1}}{\Delta t} = k_{PCM}\cdot\left(0 - \frac{T_n^t - T_{n-1}^t}{\Delta x^2}\right) \tag{17}$$

where Δt is the time increment between two time steps, and its value is the same as the experiments' sampling period. Note that the superscript t refers to the current time step, whereas $t-1$ implies the previous time step. If the duration of the experiment is τ, the number of times steps N_t in which the nodal equations must be solved is:

$$N_t = \tau/\Delta t \tag{18}$$

The resulting matrix equation for the unknown temperature field is solved using the Gauss-Seidel iterative method. The stopping criterion used is the scaled residual of the temperature field with a tolerance of 10^{-10}:

$$\frac{\sqrt{N\sum_{n=1}^{N}\left(T_{n,new}^t - T_{n,old}^t\right)^2}}{\sum_{n=1}^{N} T_{n,new}^t} \le 10^{-10} \tag{19}$$

where the subscripts *new* and *old* refer to the current iteration and the precedent iteration, respectively. The value of 10^{-10} has been selected for the tolerance as it provides accurate results of the temperature field without increasing computational time.

Table 2
Parameters of the genetic algorithm.

Parameter	Value
Population size	200
Elite count	10
Crossover fraction	0.8
Mutation rate	0.15
Maximum number of generations	1600
Function tolerance	$1{\cdot}10^{-5}$
Maximum number of stall generations	150

2.3.2. *Inverse problem*

The direct heat transfer problem needs as input the thermophysical properties of all materials involved, as well as initial and boundary

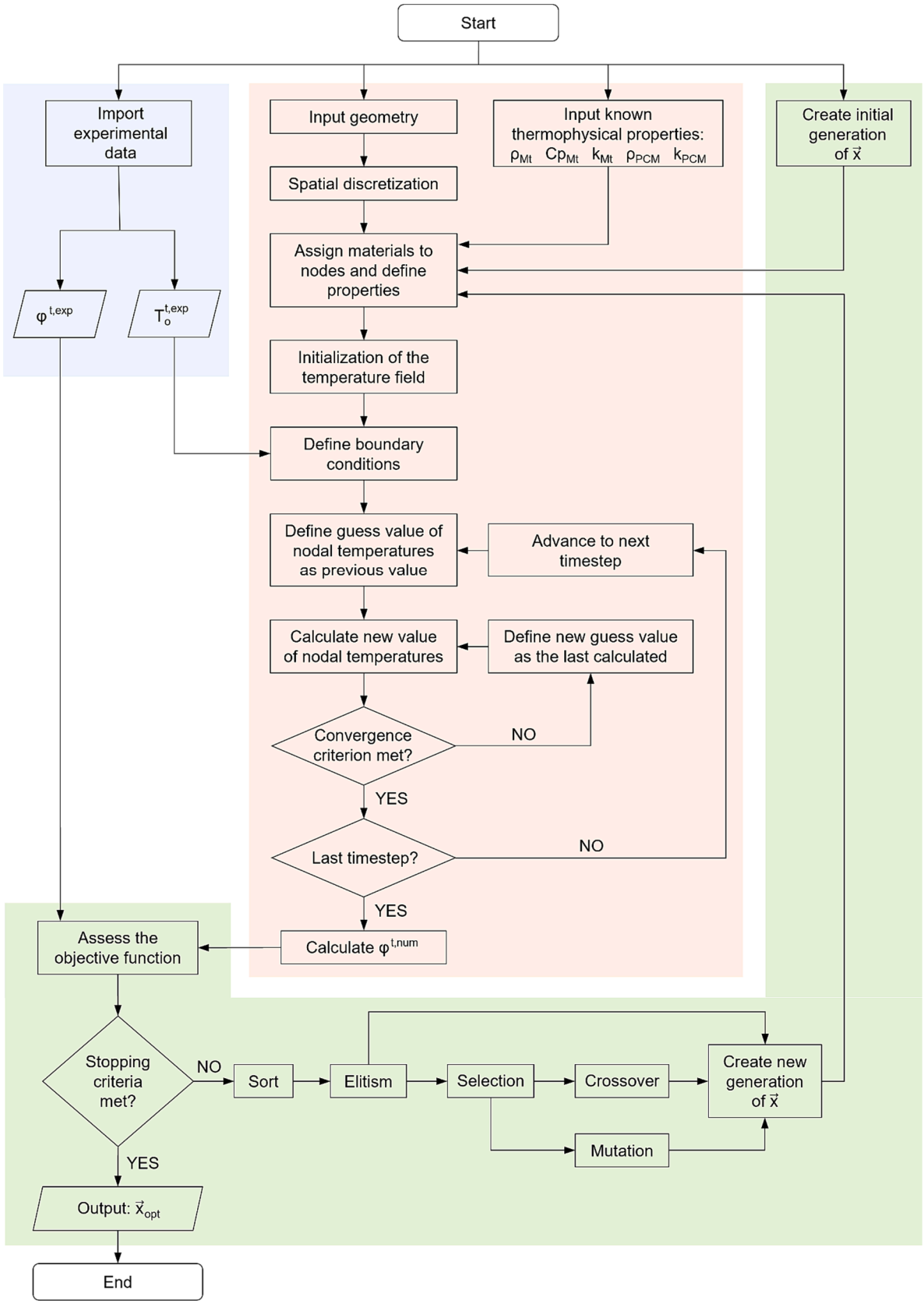

Fig. 7. Flow diagram of the computational procedure: experimental part (blue), direct FDM model (orange) and GA operations (green). (For interpretation of the references to colour in this figure legend, the reader is referred to the web version of this article.)

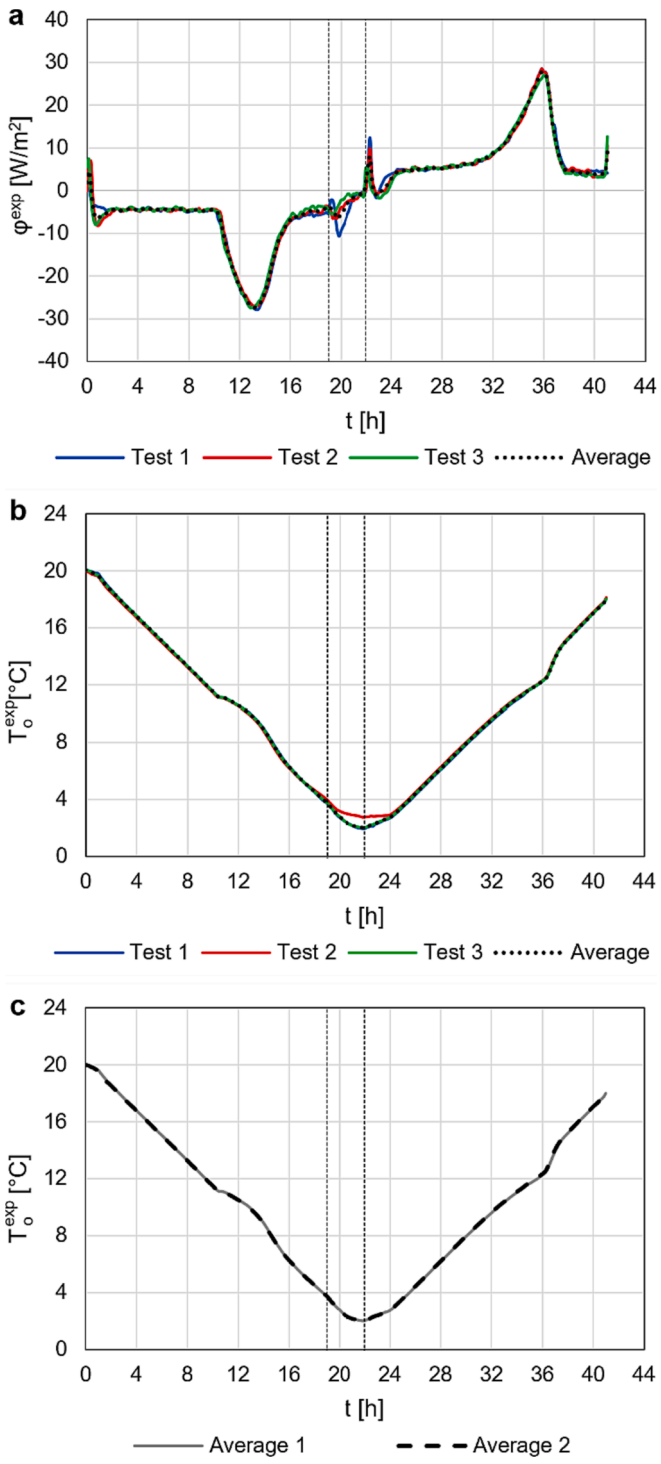

Fig. 8. Experimental results of RT11-HC for α = 1 °C/h: (a) heat flux, (b) surface temperature on one of the sides of the panel and (c) average surface temperature on each side.

conditions, so that the temperature field might be determined. However, the effective heat capacity of the PCM panels is unknown, and its determination is indeed the aim of this work.

Thus, the inverse method is employed. In this work, the experimentally measured temperature on the surface of the mortar T_o^{exp} is used as input for the direct model as the boundary condition. An optimization algorithm determines the optimum set of parameters that define the $Cp_{eff}(T)$ curve, $\vec{x}_{opt}$, that minimize the difference between the experimental the numerical heat flux at each time step. Numerical heat flux φ^{num} is calculated according to Eq. (20) at each time step, based on the nodal temperatures calculated by the direct model.

$$\varphi^{t,num} = -k_{Mt} \cdot \frac{T_1^{t,num} - T_o^{t,num}}{\Delta x/2} \equiv -k_{Mt} \cdot \frac{T_1^{t,num} - T_o^{t,exp}}{\Delta x/2} \tag{20}$$

More specifically, the inverse method looks for the optimum set of parameters that minimizes an objective function, *OF*. In this analysis, *OF* is based on the root mean square difference (*RMSD*) between $\varphi^{t,exp}$ and $\varphi^{t,num}$. Hence, the inverse method is a problem where the objective function must be minimized through an optimization algorithm. As the numerical heat flux depends on known parameters (geometry, boundary conditions, thermophysical properties) and the unknown $Cp_{eff}(T)$ curve, the inverse problem is expressed as:

Minimize:

$$OF = \sqrt{\frac{1}{N_t}\sum_{t=1}^{N_t}\left(\varphi^{t,exp} - \varphi^{t,num}\right)^2} = f(\vec{x}) \tag{21}$$

subjected to:

$$\vec{x}_{lower} \le \vec{x} \le \vec{x}_{upper} \tag{22}$$

where $\vec{x}_{lower}$ and $\vec{x}_{upper}$ are the vectors that contain the minimum and maximum values, respectively, for the optimization algorithm to create the search space. It is not strictly necessary to impose the lower and upper values linear constraint, but, if correctly chosen, they accelerate the convergence of the optimization process.

The optimization algorithm employed in this work is the genetic algorithm (GA), a metaheuristic evolutionary technique developed by J. H. Holland [43], inspired by Darwin's theory of evolution and Mendel's inheritance theory that has gained popularity lately. Evolutionary algorithms have been recently used for solving this kind of non-linear problems, as they find solutions in large and complex search spaces [44]. The GA does not require gradient information, so it is able to tackle complex and discontinuous problems. This is, this algorithm does not require differentiability of the objective function like classical optimization algorithms such as gradient descent [45]. The GA explores the search space more effectively due to its stochastic nature, increasing the likelihood of reaching the global optimum. It is population-based, implying it might be implemented in parallel [46]. Additionally, its simplicity, flexibility and robustness make it appropriate for a wide range of applications and case studies [47].

The GA is a procedural algorithm originally based on three operations: selection, crossover and mutation. Subsequently, elitism was adopted as a mechanism for retaining the best solutions between generations, improving the performance and accelerating convergence. The steps are:

1. Generation of an initial population of individuals with randomly assigned input variables ($\vec{x}$).
2. Assessment of the fitness (reciprocal of the objective function).
3. Sort the individuals in decreasing order of fitness.
4. Elitism: a sly number of the fittest individuals (elite count) is automatically passed onto the next generation.
5. Selection: from the non-elite individuals, the fittest parents are chosen, whose information will be used for creating the new offspring individuals.
6. Crossover: a percentage of the selected parents (crossover fraction) are combined to create new individuals.
7. Mutation: the remaining selected parents are randomly and individually modified to create the last new individuals.
8. Creation of a new generation by combining elite, crossover and mutation offspring.
9. Repetition of steps 2 to 8 until the stopping criteria are met: either the maximum number of generations is exceeded or the average

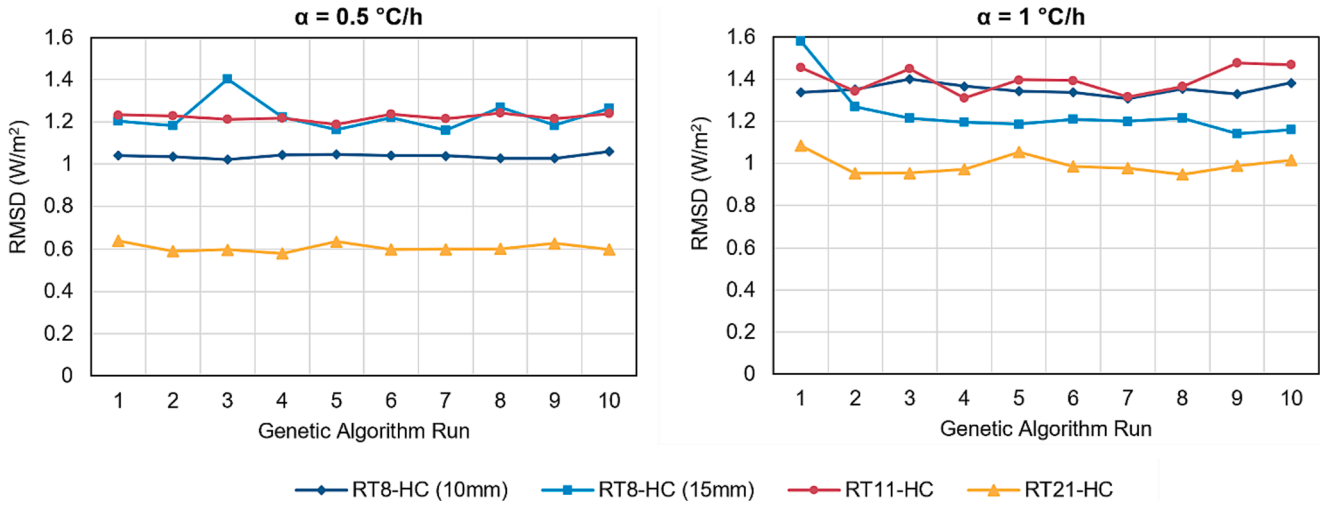

Fig. 9. RMSD of each run of the genetic algorithm of each PCM and for each temperature variation rate.

relative change in the best fitness value is less than or equal to function tolerance over a maximum number of stall generations.

The parameters of the genetic operations performed by the algorithm significantly influence the performance of the solver. Frequent population sizes are 50 individuals and maximum number of iterations range from 50 to 100 [44]. To ensure that the genetic algorithm finds the global optimum, the parameters defined in Table 2 were selected.

The mutation rate used in this work is also greater than other values reported in previous woks of genetic-algorithm-driven inverse method applied to heat transfer problems of 0.05 [48]. A flow diagram of the whole computational process of the inverse method is presented in Fig. 7, where the blue region refers to the experiments, the orange region sums up the direct mathematical model and the green region specifies the GA operations.

In order to avoid falling in local optimums, it is important to run the genetic algorithm several times [44]. This checks its robustness on finding the global optimum. Robustness and globality of the solution are fulfilled if there exists low variability in the set of solutions. In this work, the genetic algorithm was run 10 times for each PCM, and for each temperature variation rate. The optimum global solution was set as the one that provided the least RMSD.

A computational cluster with 96 GB RAM memory was used for running genetic algorithm optimization. Intel Xeon processor with 2 sockets and 8 parallel computing nuclei. In this work, six nuclei were used to reduce computation time.

3. Results and discussion

3.1. Experimental results

As it has been described in section 2.2, 3 repetitions were performed for each PCM panel (for each temperature variation rate), where surface heat flux and temperature were measured. On top of that, surface temperature was measured with two thermocouples, one on each surface. As such, in this section, it is firstly assessed the repeatability of the tests and the symmetry of the temperature distribution. Experimental results of the RT11-HC panel for the temperature variation rate of 1 °C/h have been chosen to illustrate these aspects and are shown in Fig. 8. Experimental results of the remaining panels and temperature variation rates will be displayed along results of the inverse problem solution in subsection 3.2.

Fig. 8 **(a)** shows the surface heat flux measured on each test, as well as the average value. Sensible heat exchange periods are identified by constant values of heat flux, whereas the phase change is denoted by the bell-shaped curves. Positive values mean that heat flows towards the panel and thus correspond to the melting process, whereas negative heat flux relates to the solidification process. Fig. 8 **(b)** displays the surface temperature (on one of the sides of the panels) in each test, plus the average value. In this case, sensible heat exchange is identified by constant slope regions, and the phase change by the instants where temperature variation is not linear.

Repeatability of the experimental procedure was assessed by comparing measurements from each test. It is observed that no significant variation exists in surface heat flux nor temperature from different tests, see Fig. 8 **(a) and (b)**. Besides, differences in surface temperature measurements were assessed for each panel, as two thermocouples were used, one on each surface. The average difference between thermocouples computed for all cases was negligible. In consequence, it is concluded that the same results were obtained on both sides of the panels and that the experimental setup provided a high level of repeatability. This is illustrated in Fig. 8 **(c)**, where the average surface temperatures recorded by each thermocouple are shown. As a result, for the inverse problem, the average surface temperature (average of all tests and both sensors) was set as input and average heat flux was employed for comparing by the objective function.

It is highlighted in Fig. 8 that the only variability between tests is found in the moments where the climatic module shifts from varying the temperature to stabilizing it and vice versa. These moments have been highlighted with dashed vertical lines. Thus, the variability is due to the behavior of the climatic module, which injects hot or cold air abruptly, leading to sudden variations in surface temperature and heat flux. This also explains the abrupt peaks of heat flux measured around these instants, which are not provoked by the phase change and do not influence the performance of the test. As a result, these periods were neglected for the inverse problem-solving stage. This is, the GA does not seek to minimize the objective function around these time intervals.

3.2. Numerical results

3.2.1. Genetic algorithm optimization and computational performance

To ensure that the solution found by the genetic algorithm is the global minimum of the problem, it was run 10 times on each PCM and for each temperature variation rate. The computed RMSD on each of these runs is shown in Fig. 9. There is low variability in the RMSD values regardless of the PCM and the temperature variation rate. This reveals the robustness in finding the global optimum and the suitability of the selected parameters for the genetic operations.

The average number of generations that the GA needed to create to reach the x_{opt} was 726 for the cases of temperature variation rate of

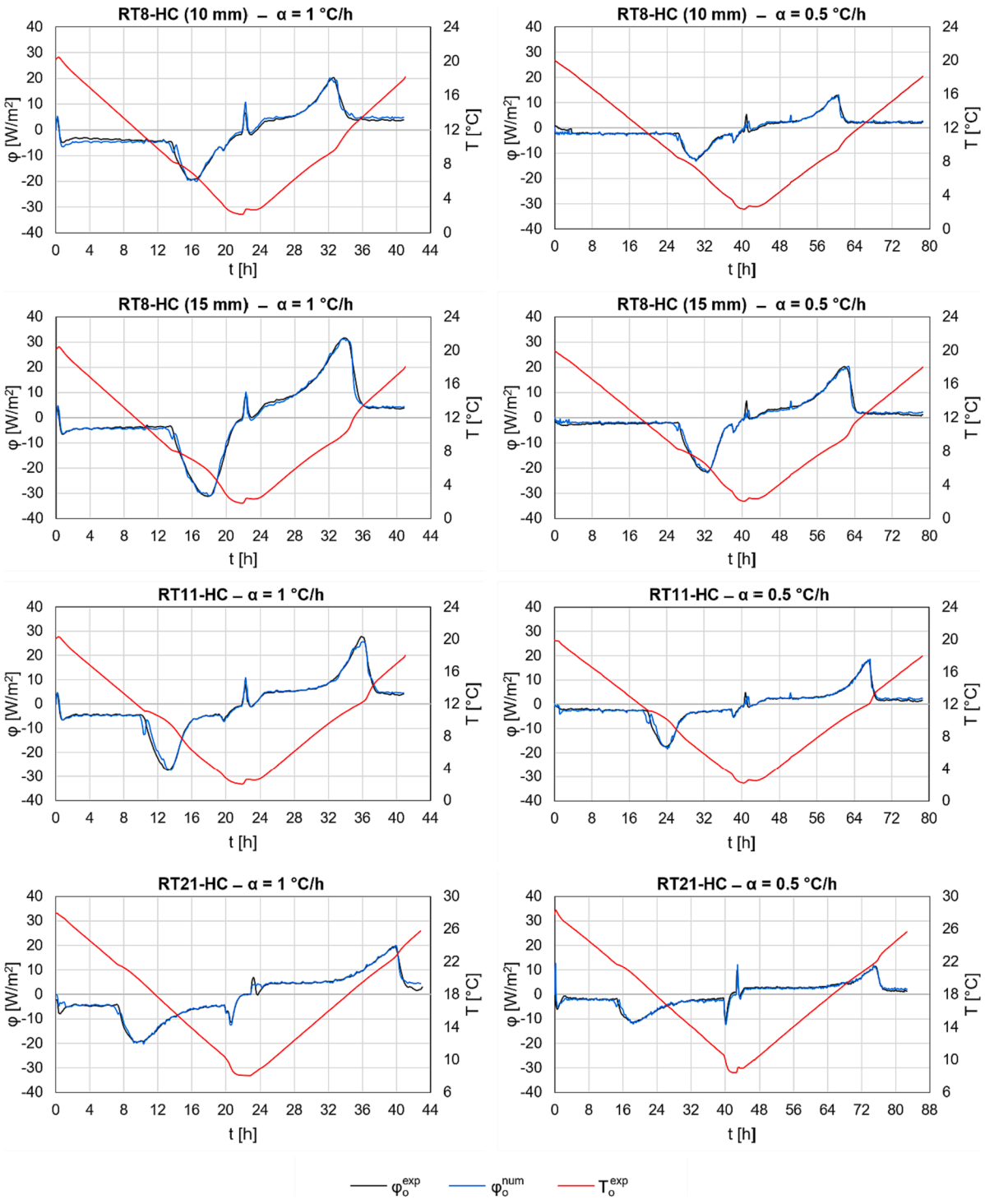

Fig. 10. Comparison of experimental heat flux and the numeric heat flux obtained by the GA/FDM-based coupled model using the experimental surface temperature as input.

Table 3
RMSD obtained from the inverse problem solution in $W/m^{2.}$

α	RT8-HC (10 mm)	RT8-HC(15 mm)	RT11-HC	RT21-HC
1 °C/h	1.060	1.130	1.214	1.246
0.5 °C/h	0.543	0.791	0.877	0.649

0.5 °C/h, and 912 for 1 °C/h. Total calculation time needed for each of the ten runs of the genetic algorithm was 3.33 h for the cases of temperature variation rate of 0.5 °C/h, and 5.54 h for 1 °C/h.

3.2.2. *Results of the GA/FDM-based coupled model*

Heat flux obtained with the developed finite difference model after GA optimization and experimental heat flux are shown in Fig. 10. Surface temperature used as input for the inverse model is also included. It is observed that the developed model thoroughly fits the experimental results during the phase change, as well as in sensible heat exchange

Table 4
Parameters of Cp_{eff} for α = 1 °C/h.

	RT8-HC (10 mm)		RT8-HC (15 mm)		RT11-HC		RT21-HC	
	S	M	S	M	S	M	S	M
Cp_S [J/kg K]	1151.43	1151.43	1999.96	1999.96	1848.49	1848.49	964.36	964.36
Cp_L [J/kg K]	1000.08	1000.08	1535.15	1535.15	1003.00	1003.00	704.12	704.12
ΔC^h [J/kg K]	29178.66	30894.02	38121.78	34641.94	45923.55	45191.55	21031.63	22171.41
σ_S^h [K²]	−2.17	−0.55	−4.84	−0.62	−2.40	−1.56	−14.54	−4.98
σ_L^h [K²]	−0.12	−0.72	−0.11	−2.34	−0.10	−0.33	−0.10	−0.42
T_p^h [°C]	8.00	8.89	7.79	8.67	10.99	11.75	21.41	22.06
$\Delta C^{\swarrow}$ [J/kg K]	67985.91	74988.19	53772.60	42710.32	67181.39	61917.69	12770.11	30858.32
$\sigma^{\swarrow}$ [K²]	−15.81	−8.32	−10.14	−16.32	−13.04	−17.84	−18.36	−16.92
$T_p^{\swarrow}$ [°C]	11.40	11.91	9.28	11.79	13.96	16.00	20.20	24.21
T_{sw} [°C]	1151.43	1151.43	1999.96	1999.96	1848.49	1848.49	964.36	964.36

Table 5
Parameters of Cp_{eff} for α = 0.5 °C/h.

	RT8-HC (10 mm)		RT8-HC (15 mm)		RT11-HC		RT21-HC	
	S	M	S	M	S	M	S	M
Cp_S [J/kg K]	1000.09	1000.09	1999.90	1999.90	1504.31	1504.31	1221.49	1221.49
Cp_L [J/kg K]	1000.11	1000.11	1200.07	1200.07	1000.15	1000.15	719.78	719.78
ΔC^h [J/kg K]	34899.62	36055.75	43833.90	39696.43	54367.54	59844.96	26875.26	26202.28
σ_S^h [K²]	−1.59	−1.00	−3.29	−1.17	−1.63	−1.08	−4.07	−2.69
σ_L^h [K²]	−0.10	−0.24	−0.14	−1.09	−0.10	−0.11	−0.12	−0.17
T_p^h [°C]	8.15	8.95	7.87	8.71	11.06	11.68	21.42	21.69
$\Delta C^{\swarrow}$ [J/kg K]	73797.06	64224.33	65070.42	76098.70	12581.91	27601.47	34549.00	39511.82
$\sigma^{\swarrow}$ [K²]	−16.89	−12.05	−11.66	−14.03	−8.78	−11.52	−23.59	−19.69
$T_p^{\swarrow}$ [°C]	11.79	12.50	10.06	12.07	10.96	13.50	23.65	25.09
T_{sw} [°C]	7.32	7.83	6.10	7.86	9.37	10.35	20.82	20.23

periods. The greatest deviations are found at the beginning and the end of the cooling and heating stages. It is highlighted that this stems from the behavior of the climatic module, that induced sudden variations of heat flux at these points. Still, simulations capture these fluctuations to a high extent. Good agreement between the numerical and experimental results indicates that the genetic algorithm finds the global solution.

RMSD computed for the studied PCM panels is shown in Table 3. These values correspond to the minimized objective function once the genetic algorithm has found the optimum set of parameters $\vec{x}_{opt}$, and for the run where the minimum RMSD was reached.

3.2.3. Effective heat capacity curves

The parameters that define the $Cp_{eff}(T)$ curves determined by the inverse method for the studied PCM panels are provided in Table 4 for 1 °C/h and in Table 5 for 0.5 °C/h temperature variation rates. The $Cp_{eff}(T)$ curves are shown in Fig. 11. In this figure, the values of the $Cp_{eff}(T)$ curves specified in the technical datasheets for the pure paraffin mixtures (determined by traditional methods) are also included. IV acronym stands for the inverse-method-determined values and DAT for the datasheet properties. Significant differences are observed between the different PCM panels: RT21-HC shows the widest curves with low effective heat capacity peaks, RT11-HC exhibits the sharpest curves and RT8-HC panels fall in between.

Comparing the results of the inverse method with different characterization velocities shows the effect of the temperature variation rate. A higher rate leads to a wider spread on the curves but with lower peaks of effective capacity, whereas lower temperature rates produce more concentrated effective heat capacity. Thus, peak effective heat capacity determined for the temperature variation rate of 0.5 °C/h was 14.59 % to 32.43 % greater than with 1 °C/h. This is due to studying the thermal behavior of whole macrocapsules, instead of small quantities of paraffins alone.

Effective heat capacity of the paraffin mixtures specified in the datasheets is sensibly greater than that of the whole macrocapsules. More specifically, the specific heat in the solid phase was up to 107.39 % higher in the datasheet values, the specific heat in the liquid phase up to 184.04 %, and the peak effective heat capacity up to 164.11 %. The greatest differences were found on RT21-HC and the, while RT8-HC (15 mm) showed the closest results to the datasheets.

It is also observed how solidification and melting curves differ: solidification occurs for a greater temperature range and peak temperature, T_p^h, is lower in solidification than in melting. This mismatch between both curves is due to hysteresis, the phenomenon that makes solidification and melting to happen at different temperatures and with unequal $Cp_{eff}(T)$ curves [49]. Generally, hysteresis is more significant in organic bio-based PCMs and hydrated inorganic salts, mainly due to supercooling and phase separation [50]. Still, even if paraffins experiment lower hysteresis, it might be significant and must be considered for thermal modeling [19]. Thus, results from the inverse method capture these differences in melting and solidification. Table 6 shows the displacement of peak temperature between melting and solidification ($T_p^{h,M} - T_p^{h,S}$) of the studied panels for the two temperature variation rates. It is observed how these values are less than 1 °C, complying with what is expected for paraffins [19]. It is also appreciated that higher temperature variation rates induce greater displacements of peak temperature. This effect is more significant in RT21-HC. As this PCM is the one with the lowest effective heat capacity, it is the most affected by changes in the temperature variation rate.

The effect of the PCM mass is observed comparing RT8-HC panels. Even if both panels contain the same substance, PCM mass over the total mass of the panel is higher for the 15 mm panel, see Table 1. As such, it possesses greater latent energy content per mass unit, leading to wider and higher $Cp_{eff}(T)$ curves. More specifically, the peak effective heat capacity of the 15 mm RT8-HC panel was from 10.10 % to 30.65 % greater than in the 10 mm panel. The 15 mm panel has a higher ratio of mass of PCM to total mass of the macrocapsule (PCM + air + aluminum) than the 10 mm panel. This means that the latent energy content per mass unit in the 15 mm panel is higher and, as a consequence, the

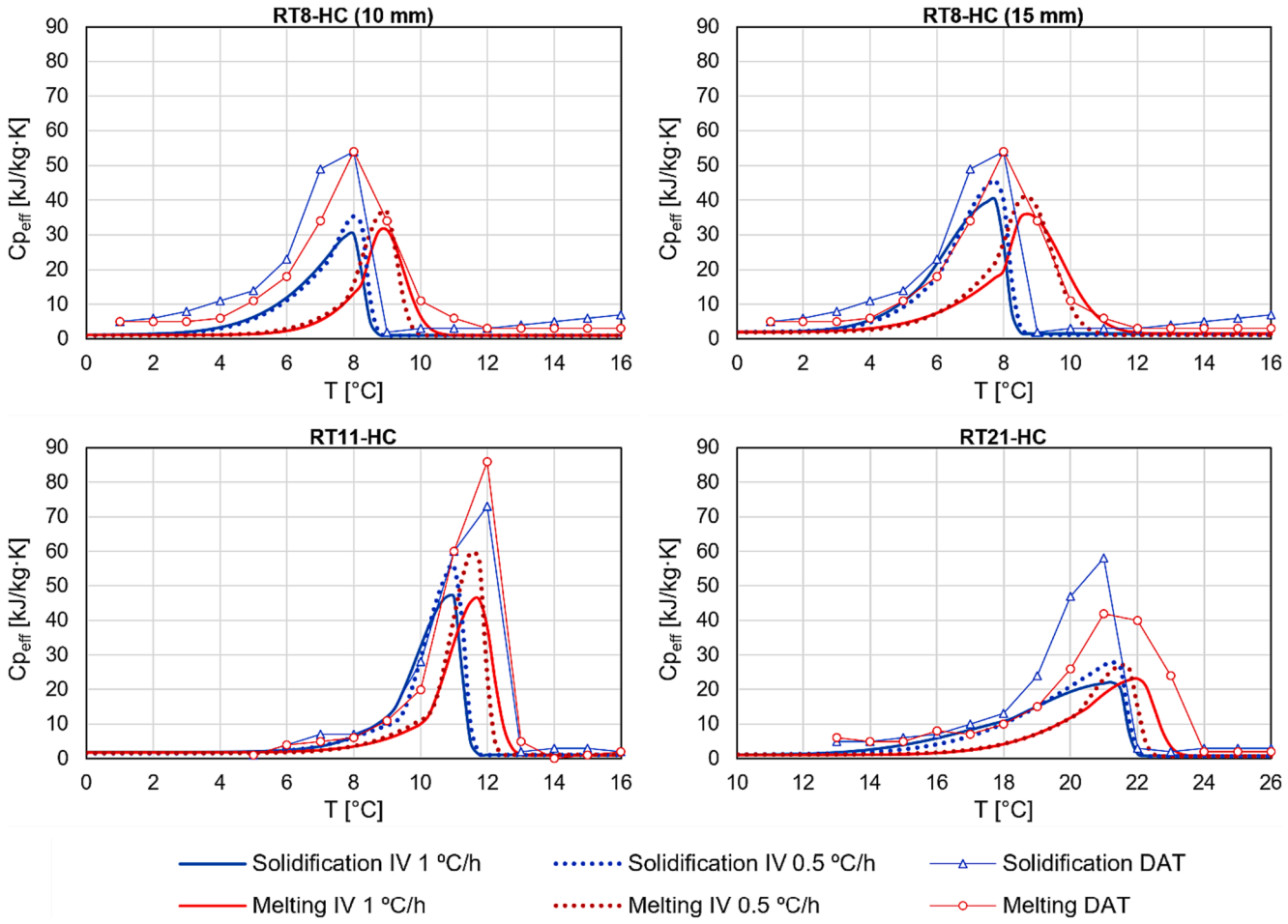

Fig. 11. Effective heat capacity of the studied PCM panels: results obtained with the inverse method applied to the whole macrocapsule and values specified in the technical datasheets for the paraffins alone.

Table 6
Displacement of T_p^h between melting and solidification in [°C].

α	RT8-HC (10 mm)	RT8-HC (15 mm)	RT11-HC	RT21-HC
1 °C/h	0.891	0.884	0.753	0.650
0.5 °C/h	0.794	0.839	0.616	0.250

$Cp_{eff}(T)$ curve in this panel reaches higher values, and with a wider spread in the temperature range. Besides, convection affects the thermal response, and a greater mass of PCM in wider panel modify the convection pattern of the liquid phase. This highlights the relevance of the mass of PCM that is characterized and the scale effect.

3.2.4. *Enthalpy-temperature curves*

Once the effective heat capacity has been identified through inverse modeling, the enthalpy-temperature curve, $h(T)$, might be determined for the PCM panels by integrating:

$$h(T) = \int_{T_{ref}}^{T} Cp_{eff}(T) \cdot dT \tag{23}$$

where T_{ref} is the reference temperature used for setting the zero-enthalpy value and, in this work, has been established as 0 °C for convenience. Results of this integration are shown in Fig. 12, as well as results of integrating the effective heat capacity specified in the technical datasheets.

Like in the effective heat capacity curves, in enthalpy curves sensible heat exchange and latent heat exchange processes might be identified. Constant slope periods correspond to sensible heat exchange (thus, the PCM is either solid or liquid), whereas the region where enthalpy increases abruptly for a narrow temperature range corresponds to the phase change.

It is observed that for RT8-HC (10 mm) and RT21-HC, there exists a gap between solidification and melting enthalpy for the liquid phase. Phase change enthalpy is greater for solidification than for melting. This is a consequence of having different $Cp_{eff}(T)$ curves for solidification and for melting in these PCMs. Note that for RT8-HC, this difference is appreciated only in the 10 mm panel, thus indicating that the mass of the encapsulated PCM greatly affects the phase change behavior.

Focusing on the region of phase change, for a given value of enthalpy, there exists a temperature difference between solidification and melting. These differences are greater for higher temperature variation rates. The greatest difference occurs in RT21-HC, whereas the lowest happens in RT11-HC. This implies that hysteresis effects on whole PCM panels are less severe in those cases where the phase change temperature range is narrower.

The specific enthalpy from datasheets exceeds the inverse-method-determined values. Deviances increase with higher temperatures. The values of peak heat capacity and specific heat of the liquid phase are greater in the datasheets than for the ones seen in the whole macrocapsule. Thus, at 30 °C, the specific enthalpy determined by traditional methods is at least 61.25 % higher (in RT8-HC (15 mm)), and up to 175.55 % higher (in RT8-HC (10 mm)).

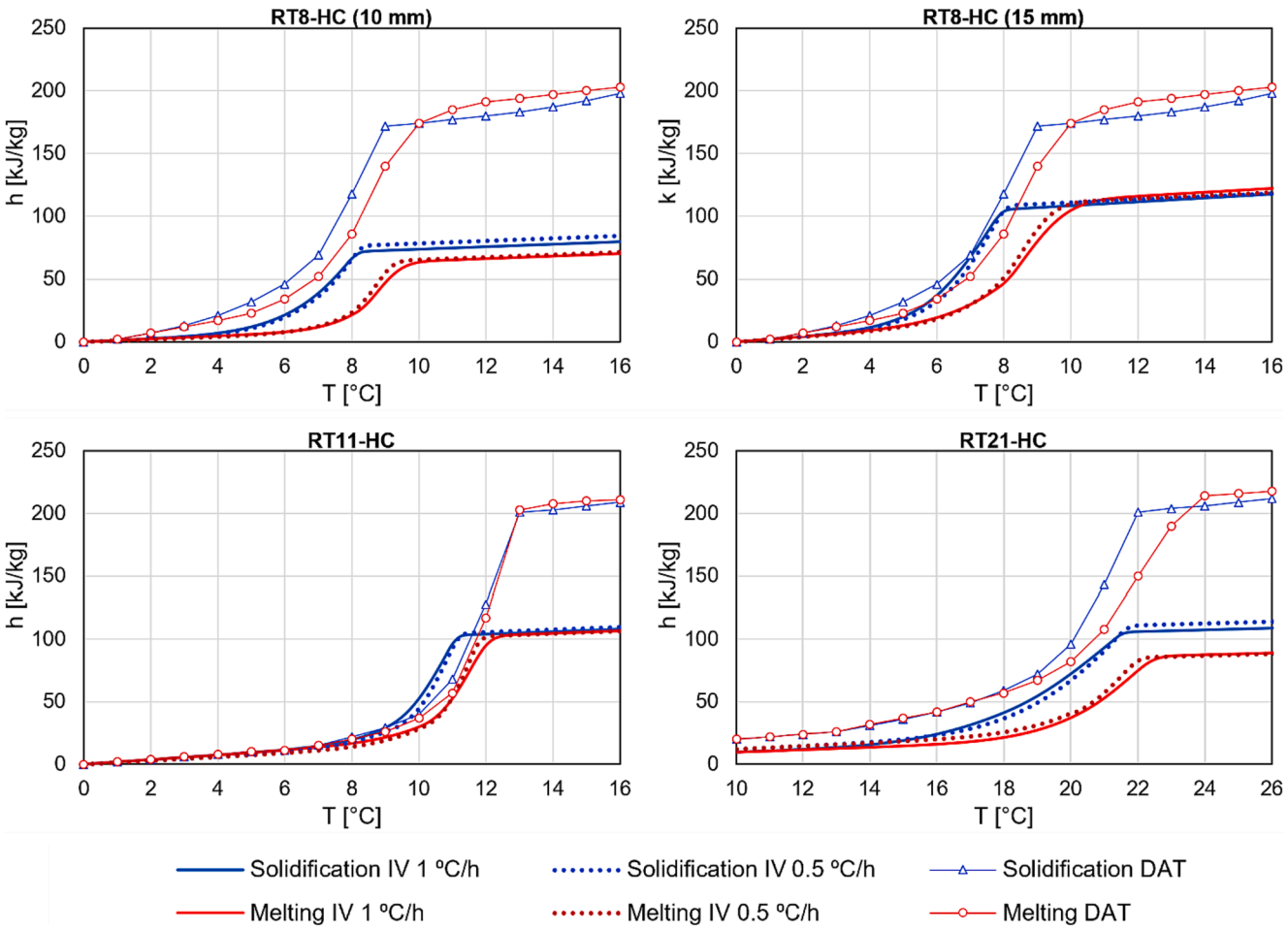

Fig. 12. Enthalpy-temperature relationship of the studied PCM panels: results obtained with the inverse method applied to the whole macrocapsule and values specified in the technical datasheets for the paraffins alone.

4. Conclusions

In this work, a one-dimensional finite difference model was developed for determining the effective heat capacity of macroencapsulated PCMs. Identification of phase change properties was performed through the inverse method coupled with the genetic algorithm. Three PCMs were tested under two temperature variation rates, 1 °C/h and 0.5 °C/h. Furthermore, for one of the PCMs, the determination of the effective heat capacity was carried out for two thicknesses of the macrocapsule. The main findings of this study are summed up accounting for the experimental and numerical results:

- The main contribution of this work is a numerical model based on the effective heat capacity method for macroencapsulated PCMs. This model is validated through the inverse method determination of the effective heat capacity of whole PCM macrocapsules. A novel curve based on the superimposition of two Gaussian curves for capturing the thermal response of PCM macrocapsules was proposed. This yields numerical results that fit thoroughly the experimental measurements, especially in the phase change regions. RMSD between numerical and experimental heat flux was 0.543 – 1.246 W/m^2, demonstrating a high level of fitness. This shape of the effective heat capacity could be applied to any other PCM whose phase transition is characterized by a single peak. Simulations also reproduce the sudden fluctuations in heat flux due to the behavior of the climatic module to a great extent. This indicates that the same model could be used for higher temperature variation rates with no loss of accuracy. It replicates the highly non-linear mechanism of phase change, which depends on multiple variables.
- Another relevant contribution is the determination of the effective heat capacity of full-scale macrocapsules. The present work reveals that thermal characterization of macroencapsulated PCMs requires the analysis of the whole PCM panels and the use of an adequate temperature variation rate. Higher rates lead to wider phase change ranges and lower effective heat capacity peaks. Effective heat capacity was up to 32.43 % greater for 0.5 °C/h than for 1 °C/h. Besides, it was proved that the scale effect is a relevant parameter. A greater ratio of mass of paraffin to total mass of macrocapsule significantly increases the effective heat capacity. RT8-HC 15 mm panel showed an effective heat capacity up to 30.65 % greater than the 10 mm panel.
- The effective heat capacity determined for the whole PCM panels and that specified for the paraffin mixtures in the manufacturer datasheets are significantly different: the specific heat in the solid phase was up to 107.39 % higher in the datasheet values, in the liquid phase up to 184.04 %, and the peak effective heat capacity, up to 164.11 %. This is, the value of the effective heat of the paraffin mixtures was more than twice that of the macrocapsules. This implies that the latent heat is overestimated if small quantities of PCM mixtures are analyzed with high heating rates, and not the whole panels with lower temperature variation rates.
- Finally, this work provides a numerical tool to simplify the energy modeling of building incorporating PCM panels. The methodology applied in this work leads to a robust model of whole macroencapsulated PCMs as unique construction materials. This is

especially useful for whole building energy simulation software to determine the thermal performance of adaptive envelopes with PCMs such as reduction of the energy consumption, hygrothermal comfort improvement or economic savings.

CRediT authorship contribution statement

Matias Alvarez-Rodriguez: Conceptualization, Data curation, Formal analysis, Investigation, Methodology, Software, Validation, Visualization, Writing – original draft, Writing – review & editing. **Mar Alonso-Martinez:** Conceptualization, Formal analysis, Funding acquisition, Investigation, Methodology, Project administration, Resources, Supervision, Validation, Writing – original draft. **Ines Suarez-Ramon:** Supervision, Visualization, Writing – review & editing. **Paulino José García-Nieto:** Formal analysis, Writing – review & editing.

Declaration of competing interest

The authors declare that they have no known competing financial interests or personal relationships that could have appeared to influence the work reported in this paper.

Data availability

Data will be made available on request.

Acknowledgements

The authors greatly appreciate the collaboration of the GICONSIME Research Group at the University of Oviedo, in particular Juan José del Coz Diaz, Full Professor at the University of Oviedo, whose support has been essential to develop this work. Furthermore, this work was supported by the Spain Ministry of Universities (FPU21/05062); the Spain Ministry of Science and Innovation through Research Projects PID2021-128056OA-I00 and RED2022-134219-T; and Foundation for the Promotion in Asturias of Applied Scientific Research and Technology though project SV-PA-21-AYUD 2021 51328.

References

[1] United Nations Environment Programme, "2022 Global Status Report for Buildings and Construction: Towards a Zero–emission, Efficient and Resilient Buildings and Construction Sector", Nairobi, 2022. Accessed: Jun. 25, 2023. [Online]. Available: https://www.unep.org/resources/publication/2022-global-status-report-buildings-and-construction.

[2] D. García-Pérez, J. Xamán, I. Zavala-Guillén, Y. Chávez-Chena, E. Simá, J. Arce, Annual evaluation of a modified wall with PCM to reduce energy consumption and CO2 emissions in Southeast Mexico, Energy Build. 292 (Aug. 2023) 113129, https://doi.org/10.1016/J.ENBUILD.2023.113129.

[3] K. Faraj, M. Khaled, J. Faraj, F. Hachem, C. Castelain, A review on phase change materials for thermal energy storage in buildings: Heating and hybrid applications, J. Energy Storage 33 (Jan. 2021) 101913, https://doi.org/10.1016/J.EST.2020.101913.

[4] L. Navarro, et al., Benchmarking of useful phase change materials for a building application, Energy Build. 182 (Jan. 2019) 45–50, https://doi.org/10.1016/j.enbuild.2018.10.005.

[5] U. Berardi, A.A. Gallardo, Properties of concretes enhanced with phase change materials for building applications, Energy Build. 199 (Sep. 2019) 402–414, https://doi.org/10.1016/J.ENBUILD.2019.07.014.

[6] International Energy Agency, "Technology Collaboration Programme on Energy Sotrage (ES TCP). Annual Report 2022", Jun. 2023. Accessed: Jul. 25, 2023. [Online]. Available: https://iea-es.org/publications/annual-report-2022/.

[7] K. Faraj, M. Khaled, J. Faraj, F. Hachem, C. Castelain, Phase change material thermal energy storage systems for cooling applications in buildings: A review, Renew. Sustain. Energy Rev. 119 (Mar. 2020), https://doi.org/10.1016/j.rser.2019.109579.

[8] Á. De Gracia, L. Navarro, A. Castell, Á. Ruiz-Pardo, S. Álvarez, L.F. Cabeza, Experimental study of a ventilated facade with PCM during winter period, Energy Build. 58 (Mar. 2013) 324–332, https://doi.org/10.1016/j.enbuild.2012.10.026.

[9] K.O. Lee, M.A. Medina, E. Raith, X. Sun, Assessing the integration of a thin phase change material (PCM) layer in a residential building wall for heat transfer reduction and management, Appl. Energy 137 (Jan. 2015) 699–706, https://doi.org/10.1016/J.APENERGY.2014.09.003.

[10] P.K.S. Rathore, S.K. Shukla, Potential of macroencapsulated PCM for thermal energy storage in buildings: A comprehensive review, Constr. Build. Mater. 225 (Nov. 2019) 723–744, https://doi.org/10.1016/J.CONBUILDMAT.2019.07.221.

[11] Z. Liu, et al., A review on macro-encapsulated phase change material for building envelope applications, Build. Environ. 144 (Oct. 2018) 281–294, https://doi.org/10.1016/J.BUILDENV.2018.08.030.

[12] E. Meng, H. Yu, B. Zhou, Study of the thermal behavior of the composite phase change material (PCM) room in summer and winter, Appl. Therm. Eng. 126 (Nov. 2017) 212–225, https://doi.org/10.1016/J.APPLTHERMALENG.2017.07.110.

[13] P. Arumugam, V. Ramalingam, P. Vellaichamy, Effective PCM, insulation, natural and/or night ventilation techniques to enhance the thermal performance of buildings located in various climates – A review, Energy Build. 258 (Mar. 2022) 111840, https://doi.org/10.1016/J.ENBUILD.2022.111840.

[14] M.A. Izquierdo-Barrientos, J.F. Belmonte, D. Rodríguez-Sánchez, A.E. Molina, J. A. Almendros-Ibáñez, A numerical study of external building walls containing phase change materials (PCM), Appl. Therm. Eng. 47 (Dec. 2012) 73–85, https://doi.org/10.1016/j.applthermaleng.2012.02.038.

[15] V.D. Cao, T.Q. Bui, A.L. Kjøniksen, Thermal analysis of multi-layer walls containing geopolymer concrete and phase change materials for building applications, Energy 186 (Nov. 2019) 115792, https://doi.org/10.1016/J.ENERGY.2019.07.122.

[16] S.N. Al-Saadi, Z. Zhai, Modeling phase change materials embedded in building enclosure: A review, Renew. Sustain. Energy Rev. 21 (May 2013) 659–673, https://doi.org/10.1016/J.RSER.2013.01.024.

[17] P. Tittelein, et al., Simulation of the thermal and energy behaviour of a composite material containing encapsulated-PCM: Influence of the thermodynamical modelling, Appl. Energy 140 (Feb. 2015) 269–274, https://doi.org/10.1016/J.APENERGY.2014.11.055.

[18] E. Günther, S. Hiebler, H. Mehling, R. Redlich, Enthalpy of phase change materials as a function of temperature: Required accuracy and suitable measurement methods, Int. J. Thermophys. 30 (4) (Aug. 2009) 1257–1269, https://doi.org/10.1007/s10765-009-0641-z.

[19] K. Biswas, Y. Shukla, A. Desjarlais, R. Rawal, Thermal characterization of full-scale PCM products and numerical simulations, including hysteresis, to evaluate energy impacts in an envelope application, Appl. Therm. Eng. 138 (Jun. 2018) 501–512, https://doi.org/10.1016/J.APPLTHERMALENG.2018.04.090.

[20] Rubitherm Technologies GmbH, "Rubitherm - Macroencapsulation - Thermal Packs". Accessed: Mar. 10, 2023. [Online]. Available: https://www.rubitherm.eu/en/productcategory/makroverkaspelung-k%C3%BChlakkus.

[21] PCM Products Ltd, "Encapsulated Products". Accessed: Jun. 08, 2022. [Online]. Available: https://www.pcmproducts.net/Encapsulated_PCMs.htm.

[22] M. Iten, S. Liu, A. Shukla, P.D. Silva, Investigating the impact of Cp-T values determined by DSC on the PCM-CFD model, Appl. Therm. Eng. 117 (May 2017) 65–75, https://doi.org/10.1016/j.applthermaleng.2017.02.021.

[23] B. Gao, Q. Yang, W. Pan, Y. Ye, F. Yi, S. Meng, A regularization method for inverse heat transfer problems using dynamic Bayesian networks with variable structure, Int. J. Therm. Sci. 182 (Dec. 2022) 107837, https://doi.org/10.1016/J.IJTHERMALSCI.2022.107837.

[24] E. Omaraa, S. Farah, A. Alemu, W. Saman, F. Bruno, M. Liu, Mathematical modelling of heat transmission in the temperature history apparatus by using inverse method to evaluate the latent heat of high temperature PCMs, Int. J. Heat Mass Transf. 167 (Mar. 2021) 120825, https://doi.org/10.1016/J.IJHEATMASSTRANSFER.2020.120825.

[25] E. Franquet, S. Gibout, J.P. Bédécarrats, D. Haillot, J.P. Dumas, Inverse method for the identification of the enthalpy of phase change materials from calorimetry experiments, Thermochim. Acta 546 (Oct. 2012) 61–80, https://doi.org/10.1016/J.TCA.2012.07.015.

[26] B. Delcroix, M. Kummert, A. Daoud, J. Bouchard, Influence of experimental conditions on measured thermal properties used to model phase change materials, Build. Simul. 8 (6) (Jun. 2015) 637–650, https://doi.org/10.1007/S12273-015-0241-8.

[27] P. Tittelein, S. Gibout, E. Franquet, L. Zalewski, D. Defer, Identification of thermal properties and thermodynamic model for a cement mortar containing PCM by using inverse method, Energy Procedia 78 (Nov. 2015) 1696–1701, https://doi.org/10.1016/J.EGYPRO.2015.11.265.

[28] R. Cheng, M. Pomianowski, X. Wang, P. Heiselberg, Y. Zhang, A new method to determine thermophysical properties of PCM-concrete brick, Appl. Energy 112 (Dec. 2013) 988–998, https://doi.org/10.1016/J.APENERGY.2013.01.046.

[29] Y. Cascone, M. Perino, Estimation of the thermal properties of PCMs through inverse modelling, Energy Procedia 78 (Nov. 2015) 1714–1719, https://doi.org/10.1016/J.EGYPRO.2015.11.275.

[30] M. Thonon, G. Fraisse, L. Zalewski, M. Pailha, Towards a better analytical modelling of the thermodynamic behaviour of phase change materials, J. Energy Storage 32 (Dec. 2020) 101826, https://doi.org/10.1016/J.EST.2020.101826.

[31] M. Zálešák, P. Charvát, L. Klimeš, Identification of the effective heat capacity–temperature relationship and the phase change hysteresis in PCMs by means of an inverse heat transfer problem solved with metaheuristic methods, Appl. Therm. Eng. 197 (Oct. 2021) 117392, https://doi.org/10.1016/J.APPLTHERMALENG.2021.117392.

[32] M. Serikawa, K. Mabuchi, M. Satoh, Y. Nozue, Y. Hayashi, M. Yokoyama, Measurement of full-scale phase change material products considering hysteresis, Appl. Therm. Eng. 192 (Jun. 2021), https://doi.org/10.1016/j.applthermaleng.2021.116895.

[33] M. Serikawa, M. Satoh, M. Mae, Y. Nozue, Y. Hayashi, Numerical models of heat storage with respect to phase change materials considering hysteresis, J. Energy Storage 55 (Nov. 2022), https://doi.org/10.1016/j.est.2022.105758.

[34] T. Barz, Paraffins as phase change material in a compact plate-fin heat exchanger - Part II: Validation of the 'curve scale' hysteresis model for incomplete phase transitions, J. Energy Storage 34 (Feb. 2021), https://doi.org/10.1016/j.est.2020.102164.
[35] Rubitherm Technologies GmbH, "Rubitherm - PCM RT-Line". Accessed: May 27, 2021. [Online]. Available: https://www.rubitherm.eu/en/index.php/productcategory/organische-pcm-rt.
[36] Rubitherm Technologies GbmH, "Macroencapslation - CSM". Accessed: Jun. 08, 2022. [Online]. Available: https://www.rubitherm.eu/en/index.php/productcategory/makroverkaspelung-csm.
[37] C-Therm Technologies Ltd., "TCi Thermal Conductivity Analyzer: Easy MTPS Testing". Accessed: Sep. 07, 2022. [Online]. Available: https://ctherm.com/thermal-conductivity-instruments/tci-thermal-conductivity-analyzer/.
[38] Hukseflux Thermal Sensors BV, "TRSYS20 thermal resistance measuring system". Accessed: Jul. 12, 2023. [Online]. Available: https://www.hukseflux.com/products/heat-flux-sensors/heat-flux-measuring-systems/trsys20-thermal-resistance-measuring-system.
[39] Sensirion AG, "SHT75". Accessed: Jul. 12, 2023. [Online]. Available: https://sensirion.com/products/catalog/SHT75/.
[40] The MathWorks Inc., "MATLAB version 9.14.0 (R2023a)". The MathWorks Inc., 2023. Accessed: Jun. 02, 2023. [Online]. Available: https://www.mathworks.com.
[41] The MathWorks Inc., "Global Optimization Toolbox version 9.14.0 (R2023a)". The MathWorks Inc., 2023. Accessed: Jun. 02, 2023. [Online]. Available: https://es.mathworks.com/products/global-optimization.html.
[42] C. Beall, R. Jaffe, Concrete and masonry databook, MacGraw Hill Professional, 2003.
[43] J.H. Holland, Adaptation in natural and artificial systems: an introductory analysis with applications to biology, control, and artificial intelligence, MIT Press, 1992.
[44] Z.Z. Wang, A. Sobey, A comparative review between Genetic Algorithm use in composite optimisation and the state-of-the-art in evolutionary computation, Compos. Struct. 233 (Feb. 2020) 111739, https://doi.org/10.1016/J.COMPSTRUCT.2019.111739.
[45] J. Amar, K. Nagase, Genetic-algorithm-based global design optimization of tree-type robotic systems involving exponential coordinates, Mech. Syst. Signal. Process. 156 (Jul. 2021), https://doi.org/10.1016/j.ymssp.2020.107461.
[46] X. S. Yang, "Chapter 2 - Analysis of Algorithms", in *Nature-Inspired Optimization Algorithms*, Elsevier, 2014, pp. 23–44. doi: 10.1016/B978-0-12-416743-8.00002-6.
[47] M. Bilal, H. Pant, L.-H. Zaheer, A. Abraham, Differential evolution: A review of more than two decades of research, Eng. Appl. Artif. Intell. 90 (Apr. 2020) 103479, https://doi.org/10.1016/J.ENGAPPAI.2020.103479.
[48] M.A. Ben Taher, H. El-Otmany, T. El Rhafiki, T. Kousksou, Y. Zeraouli, Inverse method to describe crystallization of undercooled water in cold storage tank, J. Energy Storage 36 (Apr. 2021), https://doi.org/10.1016/j.est.2021.102404.
[49] L. Klimeš, et al., Computer modelling and experimental investigation of phase change hysteresis of PCMs: The state-of-the-art review, Appl. Energy 263 (Apr. 2020) 114572, https://doi.org/10.1016/J.APENERGY.2020.114572.
[50] L. Liu, X. Zhang, X. Xu, Y. Zhao, S. Zhang, The research progress on phase change hysteresis affecting the thermal characteristics of PCMs: A review, J. Mol. Liq. 317 (Nov. 2020) 113760, https://doi.org/10.1016/J.MOLLIQ.2020.113760.